

Molecular Hydrogen Excitation in Ultraluminous Infrared Galaxies¹

R.I. Davies

*Max-Planck-Institut für extraterrestrische Physik, Postfach 1312, 85741, Garching,
Germany*

A. Sternberg

School of Physics and Astronomy, Tel Aviv University, Tel Aviv 69978, Israel

M. Lehnert

*Max-Planck-Institut für extraterrestrische Physik, Postfach 1312, 85741, Garching,
Germany*

and

L.E. Tacconi-Garman

European Southern Observatory, Karl Schwarzschildstrasse 2, 85748 Garching, Germany

ABSTRACT

We report medium resolution VLT ISAAC K-band spectroscopy of the nuclei of seven ultraluminous infrared galaxies. After accounting for stellar absorption features, we have detected several molecular hydrogen (H_2) $v = 1\text{-}0$, $2\text{-}1$, and $3\text{-}2$ vibrational emission lines, as well as the HI $Br\gamma$ and He I $2^1P - 2^1S$ recombination lines. The relative H_2 line intensities show little variation between the objects, suggesting that the H_2 excitation mechanisms in the nuclei are similar in all the objects. The 1-0 emissions appear thermalised at temperatures $T \sim 1000\text{ K}$. However, the 2-1 and 3-2 emissions show evidence of being radiatively excited by far-ultraviolet (FUV) photons, suggesting that the H_2 excitation in the ULIRGs may arise in dense photon dominated regions (PDRs). We show that the line ratios in the nuclei are consistent with PDRs with cloud densities between 10^4 to 10^5 cm^{-3} , exposed to far ultraviolet (FUV) radiation fields at least 10^3 times more intense than the ambient FUV intensity in the local interstellar medium. We have constructed starburst models for the ULIRGs based on their H_2 properties, as well as on the intensities of the recombination lines. Our models provide a consistent picture of young 1-5 Myr star clusters surrounded by relatively dense

PDRs which are irradiated by intense FUV fluxes. Comparison to the inner few hundred parsecs of the Milky Way indicates that the star formation efficiency in ULIRGs is 10–100 times higher than in the Galactic Center.

Subject headings: molecular processes — galaxies: ISM — galaxies: starburst — infrared: galaxies — galaxies: nuclei — line: formation

1. Introduction

In star forming galaxies, molecular hydrogen (H_2) vibrational emission lines include some of the brightest lines in the near-infrared (1.9–2.5 μm) K-band, and have therefore been candidates for detailed studies. The H_2 lines may be used to probe the physical conditions of molecular clouds near the star forming regions. For example, the relative strengths of lines in the $v = 1 - 0$ and $v = 2 - 1$ bands allow radiative fluorescent excitation in low-density photodissociation regions (PDRs) (Black and van Dishoeck 1987; Sternberg 1988; Sternberg and Dalgarno 1989; Burton et al. 1990b; Draine and Bertoldi 1996) to be distinguished from collisional excitation in shocks or dense PDRs (Sternberg and Dalgarno 1989; Burton et al. 1990a; Chang & Martin 1991; Draine and Bertoldi 1996; Lim et al. 2002). Determining the H_2 excitation mechanism in a given source generally requires the observation of many, often weak lines, particularly since different processes (e.g. shocks vs. FUV heating) can give rise to similar intense and thermalised 1-0 emissions. This requirement has resulted in a great deal of uncertainty in the interpretation of H_2 emissions in extragalactic objects, because signal to noise limitations, the presence of bright and uneven stellar continua, and – particularly in earlier work – low spectral resolution, have meant that often only the few strongest lines could be detected.

Recent results from Gilbert et al. (2000) and Davies et al. (2000) show that these difficulties can in fact be overcome, and that detailed studies of the molecular hydrogen in extragalactic objects is possible as long as there is sufficient signal to noise to detect some of the weaker lines. Gilbert et al. (2000) observed individual star clusters in the Antennae (NGC 4038/9), which lies at a distance of only 19 Mpc. Near the embedded star-cluster located in the mid-IR peak they detected 22 H_2 transitions, including some from very high vibrational levels, extended over an area twice the size of the continuum and nebular regions. Gilbert et al. concluded that the emission lines are produced by pure radiative FUV

¹Based on observations at the European Southern Observatory VLT (67.B-0417).

fluorescence, most likely in PDRs illuminated by the young star clusters. In work on the two nuclei in Mkn 266, which at 115 Mpc is too distant to permit studies of individual star clusters, Davies et al. (2000) used stellar templates to subtract the continuum, allowing the fluxes of the weaker lines to be measured. They found that in neither case could single shock or PDR models fit the H₂ line ratios. They concluded that $\sim 70\%$ of the prominent 2.12 μm 1-0 S(1) line originates in non-dissociative shocks; and, based on morphology and energetics, that the remaining line luminosity arises in X-ray irradiated gas, FUV-pumped gas, and in dissociative shocks.

In this paper we study H₂ excitation in ultraluminous infrared galaxies (ULIRGs). Such objects often have 1-0 S(1) to Br γ line ratios greater than unity (Goldader et al. 1995; Murphy et al. 2001). In star forming regions where the 1-0 emission is produced by FUV-pumped fluorescence the 1-0 S(1)/Br γ intensity ratio is $\lesssim 1$ (e.g. Puxley et al. 1988; Doyon et al. 1994; Davies et al. 1998), suggesting that in ULIRGs the 1-0 emission is collisionally excited in hot gas leading to higher H₂ line surface brightnesses. Indeed, because the majority of ULIRGs show signs of elevated star formation rates, as well as interactions and superwinds (Sanders & Mirabel 1996), one might expect shocks or dense PDRs to play important roles in the excitation and emission processes. We have obtained spectra deep enough to detect $v = 2-1$ and $3-2$ transitions, with the goal of constraining the H₂ excitation mechanisms in the ULIRGs.

2. Observations and Data Reduction

Our data were obtained as part of the service observing programme at the *Very Large Telescope* between June and September 2001. ISAAC was used in Medium Resolution mode in the K-band, providing a nominal resolution of $R=2600$ with a 1" slit. Since the wavelength coverage in this mode is only 0.122 μm , two settings were used with an overlap of 5–10%. The total integration time was 20 minutes per setting. Standard calibrations were performed, including atmospheric standard stars (type B or G0V), arcs, flatfields, and dark frames. The data were reduced using PC-IRAF 2.11.3 using standard techniques. Wavelength calibration was achieved in two steps: the arc frames were used to apply a transformation which removed curvature and provided an initial calibration; then the sky lines on the object frames themselves were used to remove any residual tilt and fix the final calibration.

Spectra were extracted over 5 pixels (0.75"). Although in a number of cases the line emission was extended (in two cases very much so) beyond this, a short aperture was used for two reasons: (1) the slit position angles were assigned rather arbitrarily, and so to avoid biasing the analysis, we restricted the spectra to the nuclear region; and (2) the signal-to-

noise was invariably reduced if the spectra were extracted over a longer aperture, most likely as a result of the bright continuum. The two segments of the spectrum for each object were combined after applying a scaling measured from the overlapping region. The same scaling was then also applied to the reduced 2D spectra.

An approximate flux calibration was derived from the standard stars, the K-band magnitudes of which were estimated from the spectral type and V-band magnitude; there was a very good correspondance (to better than 0.1 mag) to the K-band magnitudes that could be measured directly (e.g. from the 2MASS catalogue). The K-band magnitudes are typically up to ~ 1 mag fainter than values published elsewhere. This is a result of the smaller aperture used here (e.g. Goldader et al. 1997 used 3×3 or 3×9 arcsec apertures). Similarly the 1-0 S(1) fluxes are typically a factor ~ 2 fainter than those of Goldader et al. (1997). Notably, the flux is 3 times fainter in IRAS 16164–0746 and MCG –03–04–014, but position-velocity diagrams for these objects show the line emission is very extended; on the other hand, the flux is only 50% less for IRAS 14378–3651.

Acquisition images with integration times of a few seconds were taken before each spectrum. These are shown in Fig. 1 together with the orientation of the slit across the nucleus of each object. The position angle of the slit was set to lie along the major axis of the object as determined from 2MASS K-band or red Digitised Sky Survey images. Where there was no clear axis, the slit was set east-west.

3. Continuum Fitting and Line Extraction

The weakest $v = 3-2$ lines that we have detected have strengths that are only a few percent of the 1-0 S(1) line. These are difficult to detect because they are similar in scale to the absorption features present in the stellar continua dominated by late type giant or supergiant stars. In particular the 3-2 S(5) line at $2.066 \mu\text{m}$ coincides with a bump on the continuum at $2.067 \mu\text{m}$; and the 3-2 S(3) line at $2.201 \mu\text{m}$ sits on the edge of the Na absorption at $2.207 \mu\text{m}$. To overcome these difficulties we have fitted and subtracted a continuum constructed from the stellar templates of Wallace and Hinkle (1997). This library includes over 100 K-band spectra of stars spanning spectral types O–M and luminosity classes I–V, at a resolution of $R \sim 3000$. We tried a variety of combinations of template stars, and concluded that while there was very little difference between the fits found using giants or supergiants, the dwarfs produced a noticeably poorer match to the continuum. Finally we used 7 templates of supergiants ranging in spectral type from F5 to M5. Extending the range to earlier types or increasing the number of templates used had no noticeable effect on the final result. During the fitting process, the relative scalings of these were varied to minimise

the difference between their sum and the spectrum, excluding any regions close to line emission. The resulting combination of templates was then reddened (i.e. effectively allowing adjustments to the overall slope of the continuum) using the Howarth (1983) extinction curve, and finally convolved with a Gaussian to take account of the stellar velocity dispersion. The extinction and Gaussian FWHM were allowed to vary during the minimisation. In all cases except for IRAS 16164–0746, the extinction derived in this way was small ($A_V < 1$), a result that is not surprising if the stars and dust are mixed. The results of the fitting procedure are shown in Fig. 2 as the thick lines drawn over the spectra: the fits are successful and in most cases match the observed continuum features well. This confirms that the scaling between the two segments of each spectrum is correct, and that the weak line fluxes are likely to be accurate.

Line fluxes were measured from the spectra after subtraction of the stellar continuum, and are given in Table 4. We have detected the S(2), S(1) and S(0) lines in the $v = 1\text{-}0$ band, the S(3), S(2), and S(1) lines in the 2-1 band, and the S(3) line in the 3-2 band. The transition wavelengths are listed in Table 4. We have also set upper limits for the 3-2 S(5) line intensities. In addition, in each galaxy we detected the HI 2.17 μm Br γ and the HeI $2^1P - 2^1S$ 2.06 μm recombination lines. The uncertainties quoted are measured directly from the spectra as the rms of the residual and hence are rather higher than the errors that would be estimated purely from photon noise, including as they do the effects of improper line and continuum fitting. Based on this, we have reached a mean signal-to-noise of 25σ for the 1-0 S(1) line.

It is apparent from Table 4 that although there is considerable variation in the ratios of HeI and Br γ to 1-0 S(1), the H₂ line ratios are in all cases very similar. Given the range of values which the ratios could take amongst these objects, the standard deviation in the ratio of any particular H₂ line to 1-0 S(1) of only 0.02–0.03 is small. We have therefore derived a mean set of ratios, which we also include in Table 4.

4. H₂ Excitation Diagrams and PDR Models

Given the H₂ line fluxes f (W m^{−2}) listed in Table 4, we have calculated the implied molecular column densities, $N_{vj} \equiv 4\pi f/A\Omega$, in the upper rotational-vibrational (vj) levels of the observed transitions, where A is the radiative rate and $\Omega = 0.75''^2$ is our aperture size. We assume that the quadrupole transitions are optically thin and we use the radiative A values as given by Wolniewicz et al. (1998). In Figs. 3 and 4 we show plots of $\log N_{vj}/g_{vj}$ (where g_{vj} is the statistical weight) vs. the energy (in K) of each observed vj level. We have normalized the population distributions relative to $N_{1,3}/g_{1,3}$ as inferred from the 1-0 S(1)

line.

For thermalised populations at fixed gas temperature the $\log N/g$ points should lie on a straight line in the excitation diagrams. Clearly, such single component models do not fit the data. While the $v = 1$ levels appear to be thermalized at $T \sim 1300$ K, inclusion of the $v = 2$ levels raises the best-fitting temperature to $T \sim 2400$ K. Even at this temperature, however, the $v = 3$ levels remain underpopulated, and the excitation temperature inferred from the relative populations in the $v = 2$ and $v = 3$ levels exceeds 5000 K. At such gas temperatures the molecules would be rapidly dissociated, suggesting that a non-thermal excitation mechanism is responsible for the excitation of the $v = 2$ and $v = 3$ levels.

Collisional excitation in shocks could possibly account for the 1-0 emissions. A line intensity of $10^{-7} \text{ W m}^{-2} \text{ sr}^{-1}$ is equivalent to a flux of $2 \times 10^{-18} \text{ W m}^{-2}$ for our $0.75''^2$ aperture, consistent with the fluxes given in Table 2. It is only in models of non-dissociative C-shocks with velocities $\gtrsim 25 \text{ km s}^{-1}$ and preshock densities $\gtrsim 10^4 \text{ cm}^{-3}$ that the predicted 1-0 S(1) intensity reaches such values (Burton et al. 1990a; Timmermann et al. 1998; Wilgenbus et al. 2000). In C-shocks at speeds lower than this, and in all realistic J-shocks, the 1-0 S(1) intensity is significantly lower. In C-shocks at or above this speed (and for gas densities $> 100 \text{ cm}^{-3}$) the post shock temperatures are of order 1000 K. Such models would have difficulty in accounting for the relatively large columns in the $v = 2$ and $v = 3$ levels. Furthermore, for shocked emission the ortho-to-para ratio in vibrationally excited levels should attain an equilibrium value of 3 (Timmermann et al. 1998; Wilgenbus et al. 2000).

In contrast to shocks, the observed H_2 excitation could be produced in dense PDRs. In such clouds, FUV irradiation can heat the gas to temperatures ~ 1000 K, leading to collisionally excited and thermalized 1-0 line emissions, while direct FUV-pumping maintains non-thermal fluorescent populations in higher-lying vibrational levels (Sternberg and Dalgarno 1989; Burton et al. 1990b; Draine and Bertoldi 1996). In fact, a high vibrational excitation temperature, such as the 5000 K inferred from the relative $v = 3$ and $v = 2$ populations, is a basic characteristic of FUV-pumped fluorescent emission (Black and van Dishoeck 1987; Sternberg 1988). Furthermore, an additional signature of fluorescent excitation appears to be present in our data set. For those objects in which the $v = 2 - 1$ S(1), S(2), and S(3) lines were detected, the resulting N/g values for the $j = 3, 4$, and 5 levels do not appear thermalised. Instead, the $j = 4$ para-level is shifted above the adjacent $j = 3$ and $j = 5$ ortho-levels. Thus, the ortho-to-para ratio for the $v = 2$ molecules appears to be out of equilibrium and suppressed below the ortho-to-para ratio of 3 obtained in local thermodynamic equilibrium (LTE) in warm gas. This behavior is precisely what is expected for excitation by FUV-pumping, in which the greater optical depths in the ortho UV absorption lines suppresses the populations in the vibrationally pumped ortho- H_2 relative to

para-H₂ (Sternberg and Neufeld 1999).

We have constructed a series of representative PDR models to determine PDR conditions and parameters consistent with the observed H₂ line ratios. For this purpose we have used the code described in Sternberg and Dalgarno (1989, 1995), and Sternberg and Neufeld (1999). Briefly, our models consist of static, plane-parallel, semi-infinite clouds that are exposed to isotropic FUV radiation fields. At each cloud depth we compute the equilibrium atomic to molecular hydrogen density ratio, $n(H)/n(H_2)$, and we solve for the steady-state population densities in the rotational and vibrational H₂ levels in the ground electronic state. In solving for the vj populations we include the effects of FUV-pumping via the Lyman and Werner bands, collisional processes with H⁺, H, and H₂, and quadrupole radiative decays.

We present a series of five representative PDR models in which we consider a range of illuminating FUV field intensities χ , relative to the FUV field in the local interstellar medium (2.1×10^{11} photons s⁻¹ m⁻², Draine 1978), and total hydrogen particle densities $n_H = n(H) + 2n(H_2)$ in the clouds. In all of the models except model 1 (for which we keep the temperature constant at $T = 100$ K), we assume that the gas temperature varies with cloud depth as

$$T = \frac{T_{\max}}{1 + 39 \times (2n(H_2)/n_H)^5} \quad (1)$$

where $T_{\max} \sim 10^3$ K is the temperature at the cloud edge. For such thermal profiles the gas temperature equals T_{\max} in the outer atomic zone of the PDR, and then declines significantly to ~ 25 K as the gas becomes molecular. This behavior is consistent with theoretical expectations for dense PDRs, and is also empirically based (e.g. the Galactic star forming cloud S140, as analyzed by Timmermann et al. (1996) and Sternberg and Neufeld (1999)).

We summarize the parameters for our five models in Table 3. The level populations from the models are given in Table 4 (below the observed values), and are plotted in Figure 3. Also shown in the figure are the populations derived from the mean observed line ratios. We now give a short summary of the models and how well they describe the mean observed line ratios:

model 1 Low density, $n_H = 10^3$ cm⁻³, and cool (isothermal) $T = 100$ K gas, excited by a relatively weak $\chi = 10^2$ FUV field. This results in low surface brightness H₂ emission, with $I_{1-0S(1)} = 1.3 \times 10^{-9}$ W m⁻² sr⁻¹. The population ratios, including the $v = 1$ levels are characteristic of pure radiative fluorescent excitation, unaffected by vibrational collisional excitation or deexcitation. This model does not produce a good fit to the data.

model 2 The gas density and UV field are both increased by an order of magnitude to

$n_{\text{H}} = 10^4 \text{ cm}^{-3}$ and $\chi = 10^3$, and a thermal profile as given by Eq. 1 is adopted with $T_{\text{max}} = 10^3 \text{ K}$. This results in much higher line surface brightnesses, especially for the 1-0 transitions, with $I_{1-0\text{S}(1)} = 5.2 \times 10^{-8} \text{ W m}^{-2} \text{ sr}^{-1}$. The $v = 1$ levels are thermalised by collisions, while the $v = 2$ & 3 levels are excited by FUV-pumping and therefore display the ortho-to-para shifts characteristic of fluorescent excitation (Sternberg and Neufeld 1999). This model matches the data rather well, showing that the H_2 populations are consistent with those expected for dense PDRs with hot outer boundaries.

model 3 Similar to model 2, with again $n_{\text{H}} = 10^4 \text{ cm}^{-3}$ and $\chi = 10^3$, but with T_{max} increased to 2000 K. This increases the surface brightnesses in the 1-0 lines still further, with $I_{1-0\text{S}(1)} = 2.0 \times 10^{-6} \text{ W m}^{-2} \text{ sr}^{-1}$. The higher v levels are now also thermalised and therefore have much lower populations relative to the $v = 1$ level. The result is very similar to a simple purely “thermal” model in which the populations are assumed to be in LTE at 2000 K, and very much under-predicts the $v = 2$ & 3 populations.

model 4 Also similar to model 2, with $n_{\text{H}} = 10^4 \text{ cm}^{-3}$ and $T_{\text{max}} = 10^3 \text{ K}$, but with the UV field increased by a factor of 100 to $\chi = 10^5$. The relative populations and line intensities are hardly affected compared to model 2, and there is only a slight increase in the populations of the higher v levels.

model 5 As in model 4, having $\chi = 10^5$ and $T_{\text{max}} = 10^3 \text{ K}$, but with the gas density increased by a factor of 100 to $n_{\text{H}} = 10^6 \text{ cm}^{-3}$. The higher density leads to more effective thermalisation in the higher v levels, so that these levels are under predicted by the model, although not as severely as in model 3.

It is clear that models 2 and 4 provide the best match to the mean line ratios, and that with the current data they are effectively indistinguishable. The 1-0 S(1) line intensities of the 2 models are also similar, and consistent with those observed in the ULIRGs.

In our models we have not explicitly computed the heating and cooling balance that would be expected to yield hot gas in the outer photodissociated atomic zones. In PDR theory the 6–13.6 eV photons are available for heating via photoelectric emission from dust grains, and collisional deexcitation of FUV-pumped H_2 . For our model 2, the total energy flux in this band is $2.6 \times 10^{-3} \text{ W m}^{-2}$; while the emergent flux in the H_2 1-0 S(1) line is $5.2 \times 10^{-8} \text{ W m}^{-2}$, or 2×10^{-5} of the available FUV energy, a fraction consistent with theoretical computations (Sternberg and Dalgarno 1989; Burton et al. 1990b). Thus it is possible that the H_2 emission – including the thermalised $v = 1 - 0$ emissions – is produced entirely in PDRs. However, for the 1-0 lines we cannot rule out contributions from additional sources such as shock waves.

Having looked at which models might match the mean ratios, we now briefly consider the individual objects.

From surface brightness considerations alone, model 1 can be ruled out for all objects. Integrated over the $0.75''^2$ aperture in which we have measured the line fluxes, this model would predict a maximum 1-0 S(1) flux of $2.3 \times 10^{-20} \text{ W m}^{-2}$, nearly 2 orders of magnitude less than the range observed in our sample. We would also argue against model 3 because it requires that all the levels are effectively thermalised at the same temperature. We now consider the remainder of the models for each object. For IRAS 19458+0944, models 2 & 4 provide good fits to the data, and while model 5 also fits it is more to the extreme of the errorbars. These three models also match the data for MCG –03–12–002 well, although the $v = 1$ levels indicate a temperature at the edge of the clouds somewhat warmer than 1000 K. For MCG –03–04–014 models 2 and 4 also match the data well, but here the extra data point for $v = 2$ levels suggests that model 5 is less likely. IRAS 01364–1042 and IRAS 16164–0746 present some of the best data. For these objects model 5 can be confidently dismissed in favour of models 2 and 4. For the former, the $v = 1$ populations suggest, as for MCG –03–12–002, that the temperature at the edge of the clouds is slightly warmer than 1000 K. The cases for IRAS 14378–3651 and IRAS 20414–1651 are rather uncertain and models 2, 4, and 5 all match the data well; although in the latter object, there is a tendency towards the higher density model since the $v = 2$ distributions appear more thermalised.

Our conclusion from the line intensities and ratios is that all the objects can be characterised by simple single-component PDRs illuminated by FUV fields with $\chi \geq 10^3$, and hydrogen densities in the range $n_H = 10^4\text{--}10^5 \text{ cm}^{-3}$ (possibly in some cases as high as 10^6 cm^{-3}), and a temperature at the outer edge of the clouds $T = 1000\text{--}1500 \text{ K}$. Multi-component models (Burton et al. 1990b) could also be considered, in which, for example, an inner dense region is responsible for the thermalised 1-0 emissions, with contributions to the fluorescent component from more extended low density gas (see also our discussion of Orion in §4.2). However, given the limited spatial information in our data set we do not consider such models here.

Observations of additional PDR diagnostic lines such as [O II] 63 μm and 145 μm , [C II] 158 μm , or high- J CO transitions (Tielens and Hollenbach 1985; Sternberg and Dalgarno 1989; Koester et al. 1994) would provide valuable additional constraints on the PDR conditions. However, no such data is yet available for our sources.

4.1. Starburst Models

If the observed molecular hydrogen emissions are produced in PDRs then it is of interest to consider whether the FUV sources – most likely hot OB stars – can also provide the Lyman continuum (Lyc; $h\nu > 13.6$ eV) EUV photons responsible for the Br γ recombination line emission. As we will now show, the relative photon production rates in the FUV and EUV bands that are implied by the H₂ and Br γ line fluxes, are consistent with young star clusters containing populations of massive hot stars.

In Table 6 we present the results of starburst model computations using our starburst code STARS (e.g. Sternberg 1998; Thornley et al. 2000) for the Lyc and FUV-band photon rates Q_{Lyc} and Q_{H_2} produced in evolving star clusters. We define the FUV-band as spanning 912 to 1130 Å, since photons in this wavelength range can be absorbed in the H₂ Lyman and Werner absorption line systems, leading to FUV-pumped fluorescent H₂ emission lines. In Table 6 we also list the helium ionizing (HeI; $h\nu > 24$ eV) photon production rates, and the associated K-band luminosities, L_K ², and bolometric luminosities L_{bol} of the model clusters. We consider a range of cluster ages, for both instantaneous ($10^5 M_{\odot}$) bursts and continuous ($SFR = 1 M_{\odot} \text{ yr}^{-1}$) star formation, assuming Salpeter initial mass functions (IMFs) with upper-mass limits of $M_{\text{up}} = 30$ and $120 M_{\odot}$. Our starburst models incorporate hot-star “wind-atmospheres” in the computation of the cluster luminosities and spectral energy distributions (Sternberg et al. 2003). We assume solar metallicity for the evolutionary tracks and stellar atmospheres.

Table 6 shows that the ratio $Q_{\text{H}_2}/Q_{\text{Lyc}}$ varies with cluster age and also depends on M_{up} . For instantaneous bursts, $Q_{\text{H}_2}/Q_{\text{Lyc}}$ increases rapidly with age as the hottest Lyc producing O stars disappear from the system, whereas FUV photons continue to be produced by the B-stars. For continuous star formation $Q_{\text{H}_2}/Q_{\text{Lyc}}$ increases slightly with time and reaches fixed values as the relative numbers of O and B type stars reach equilibrium. At early times the photon ratio is smaller for larger M_{up} due to the efficient production of Lyc photons in the most massive stars.

We determine Q_{Lyc} for our sources from the Br γ fluxes assuming case B recombination at 10⁴ K, for which 71.9 Br γ photons are produced for every Lyc photon absorbed in photoionizations. Similarly, Q_{H_2} is proportional to the flux in a FUV-pumped fluorescent H₂ emission line. To estimate Q_{H_2} we use the flux in the the 2-1 S(3) line since this is a FUV-pumped line that we detected in every galaxy in our sample. The FUV-band to H₂

²we define L_K as the total luminosity in the 1.9–2.5 μm K-band for a frequency independent K-band flux density. If $S_{2.2}$ is the 2.2 μm flux density in mJy and D_{Mpc} is the source distance in Mpc then $L_K(L_{\odot}) = 1.17 \times 10^4 D_{\text{Mpc}}^2 S_{2.2}$. The absolute K-magnitude $M_K = -0.33 - 2.5 \log L_K$

line photon “conversion efficiency” depends on the ratio of the incident FUV intensity to gas density, χ/n_{H} , a PDR parameter that controls the fraction of the incident FUV photons absorbed by molecules as opposed to dust grains in the PDRs (Black and van Dishoeck 1987; Sternberg 1988). The efficiency is largest when $\chi/n_{\text{H}} \lesssim 0.01 \text{ cm}^3$, and decreases for larger values of the FUV to density ratio ³. We assume a FUV to 2-1S(3) conversion factor of $\eta = 4.1 \times 10^{-3}$, as given by our PDR model 2. For this model η is at about half the maximum efficiency. It follows that the distance independent ratio

$$\frac{Q_{\text{H}_2}}{Q_{\text{LyC}}} = \frac{F_{2-1\text{S}(3)}}{F_{\text{Br}\gamma}} \frac{1}{71.9 \eta} \frac{\lambda_{2-1\text{S}(3)}}{\lambda_{\text{Br}\gamma}} = 3.25 \frac{F_{2-1\text{S}(3)}}{F_{\text{Br}\gamma}}. \quad (2)$$

In Table 5 we list the FUV to LyC photon ratios, that we infer for our ULIRG sample. The ratios range from 0.3 to 0.9, with $Q_{\text{H}_2}/Q_{\text{LyC}} \approx 0.5$ a representative value.

Our starburst models thus show that the H_2 and $\text{Br}\gamma$ line emissions may be produced by the same populations of star clusters in the ULIRG nuclei. If the hydrogen molecules in the PDRs are absorbing the FUV photons at close to maximum efficiency, then the clusters must be young, as shown by the photon ratios listed in Table 6. The clusters must then also contain massive stars with M_{up} close to $120 M_{\odot}$. For instantaneous bursts, a ratio $Q_{\text{H}_2}/Q_{\text{LyC}} \approx 0.5$ implies an age of $\sim 1 \text{ Myr}$. For continuous star formation the limit on the age is less severe, and could be as large as $\sim 10 \text{ Myr}$, especially if the FUV to H_2 line conversion efficiency is smaller than we have assumed. It appears then that the same stellar radiation sources can plausibly account for both the H_2 lines and the recombination line emissions. This would not be the case if, for example, the $\text{Br}\gamma/\text{H}_2$ line intensity ratios were much larger than observed.

The $2.06 \mu\text{m}$ HeI recombination line provides an additional constraint, as this line is proportional to Q_{HeI} , the number of HeI continuum photons ($h\nu > 24.6 \text{ eV}$) produced per unit time. The strong $2.06 \mu\text{m}$ line in our spectra is a further indication of the presence of very hot and massive stars. However, as noted by Shields (1993) converting the helium line flux to Q_{HeI} depends on a variety of largely uncertain parameters for the HII regions, including the nebular densities, gas filling factors, and dust content. Here we derive a lower limit, $Q_{\text{He}}^{\text{min}}$, assuming that all of the HeI continuum photons are absorbed in helium ionizations, followed by (case-B) recombinations. The effective recombination coefficient for the $2.06 \mu\text{m}$ line (Smits 1991; Osterbrock 1989) ranges from $\alpha_{2.06}^{\text{eff}} = 4.74 \times 10^{-14} \text{ cm}^3 \text{ s}^{-1}$ at low densities (10^2 cm^{-3}), to $\alpha_{2.06}^{\text{eff}} = 6.78 \times 10^{-14} \text{ cm}^3 \text{ s}^{-1}$ at high densities (10^4 cm^{-3}), where collisional depopulation of the 2^3S level to the 2^1S and 2^1P levels (rather than photon

³The efficiency also depends on the effective FUV grain absorption cross section in the PDRs. We assume a cross section equal to $1.9 \times 10^{-21} \text{ cm}^{-2}$ as appropriate for Galactic dust (Draine 2003).

decay to 1^1S) enhances the HeI $2.06\mu\text{m}$ intensity. Given a total case-B recombination $\alpha_B(\text{HeI}) = 2.73 \times 10^{-13} \text{ cm}^3 \text{ s}^{-1}$ (Osterbrock 1989), it follows that at least 5.8 $2.06\mu\text{m}$ line photons are emitted per HeI ionizing photon ⁴. The resulting limits, $Q_{\text{He}}^{\text{min}}/Q_{\text{Lyc}}$, are listed in Table 5. They are consistent with the young ages we have inferred for the starbursts.

Without any extinction corrections, the Br γ fluxes and source distances imply Lyc emission rates ranging from $6 \times 10^{52} \text{ s}^{-1}$ (in MCG-03-12-002), to $3.4 \times 10^{54} \text{ s}^{-1}$ (in IRAS 19458+0944). For young 1 Myr instantaneous bursts this implies total stellar masses ranging from 6.7×10^5 to $3.8 \times 10^7 M_{\odot}$ for a Salpeter IMF ranging from 0.1 to $120 M_{\odot}$. The implied stellar masses increase significantly if such clusters are more evolved (c.f. Thornley et al. 2000). For continuous star formation, the Br γ fluxes imply star formation rates from 0.7 to $38 M_{\odot} \text{ yr}^{-1}$, assuming an age of 5 Myr. It follows from the starburst data in Table 6 that for young (1 Myr) instantaneous bursts the predicted K-band luminosities of clusters account for at most a few percent of the observed K-band luminosities. For continuous star formation, the fractions could be a bit larger, up to $\sim 20\%$, but are still small. We conclude that the observed K-band continua are not produced in the current star forming episode.

Equivalently one can consider the Br γ equivalent widths, which should exceed 100\AA or more for star formation with ages of 10 Myr or less. The directly measured equivalent widths, however, lie in the range $5\text{--}20\text{\AA}$ for these ULIRGs. Low Br γ equivalent widths have also been observed by other authors (Goldader et al. 1995; Murphy et al. 2001). The depth of the continuum absorption features (in Section 3 we showed that the scale of these features was similar to that in late-type giants and supergiants) suggest that it is unlikely that the K-band continua arise from hot dust associated either with starbursts or hidden AGN. On the other hand, it is plausible that the continua are produced by an older underlying population. The only firm conclusion we can draw about such a population is that it contributes little to the total FUV and ionising flux, which means that either it is at a low level or has ceased in the recent past. For evolved 10^{10} yr stellar populations, $M/L_K \approx 20$ (Thronson and Greenhouse 1988; Fig 3 of Tacconi-Garman et al. 1996), implying stellar masses of order $10^{10} M_{\odot}$. If the near-infrared continuum is dominated by a younger 10^8 yr population, consistent with that over which star formation occurs in the major merger models of Mihos and Herquist (1996), then the mass to light ratio is $M/L_K \approx 0.7$ (Tacconi-Garman et al. 1996), implying much more moderate masses in the range $10^8\text{--}10^9 M_{\odot}$. In this case, the star formation must have ceased already, since it would otherwise make a significant contribution to the observed FUV and ionising fluxes. We note that in some models of Mihos and Herquist (1996) (notably the bulgeless mergers), multiple separate epochs of star formation can be triggered during an

⁴We note that since each He recombination results in about one photon that can ionize H, we have assumed that our estimates of Q_{Lyc} are unaffected by the presence of He.

interaction, occurring at each point of closest approach as the two progenitor galaxies orbit each other before finally merging.

From Tables 5 and 6 it can also be seen that the bolometric luminosities based on the star formation rates implied by the Br γ fluxes are very much less than those inferred by the IRAS fluxes. The total correction factor needed to reconcile them is in the range 20-40. The difference could arise from a combination of aperture effects (discussed in Section 2), extinction, and perhaps also dust absorption within the nebulae as proposed for ULIRGs by Voit (1992) and Bottorff et al. (1998). Mid infrared spectroscopy by Genzel et al. (1998) indicates that values of $A_V = 5\text{--}50$ (screen model) or $A_V = 50\text{--}1000$ (mixed model) are not uncommon – i.e. for lines in the near infrared one may be seeing as little as 1–10% of the total flux. Additionally, dust within the ionised nebulae could absorb the Lyc photons. FUV photons would also be absorbed, reducing the FUV intensity at the PDR boundaries. Because the dust absorption and aperture effects can apply to the line emitting regions and older stellar population differently, it is not straight forward to correct for them and we have not attempted to do so.

Assuming that the observed H₂ emission is distributed uniformly over the 0.75''² aperture, the area averaged FUV intensities within this region are given by

$$\langle \chi \rangle = 1700 \left(\frac{Q_{H_2}}{10^{52} \text{ s}^{-1}} \right) \left(\frac{R}{100 \text{ pc}} \right)^{-2} \quad (3)$$

where R is the radius probed by our observational aperture. For our ULIRG sample, $\langle \chi \rangle$ ranges from 700 to 2000, broadly consistent with our PDR model 2.

The FUV fluxes could be substantially larger if the filling factor of the ionized and PDR gas is small. For example, we consider a collection of identical and young star clusters each surrounded by its own HII region (which does not overlap with any other), with PDRs at the outer boundaries of these HII regions. For such a system, the total Lyc emission rate $Q_{\text{Lyc}} = N_{\text{clus}}(4\pi/3)\alpha_B n_e^2 r_s^3$ where N_{clus} is the number of star clusters, n_e is the electron density in the HII regions, r_s the Strömgren radius, and α_B is the hydrogen recombination coefficient. The FUV-band flux at the edges of the PDRs is $(Q_{H_2}/N_{\text{clus}})/4\pi r_s^2$, so that the FUV flux (in units of the Draine (1978) field) may be written as

$$\chi = 3.5 \times 10^3 \left(\frac{Q_{H_2}}{Q_{\text{Lyc}}} \right) \left(\frac{Q_{\text{Lyc}}/N_{\text{clus}}}{10^{52} \text{ s}^{-1}} \right)^{1/3} \left(\frac{n_e}{100 \text{ cm}^{-3}} \right)^{4/3} . \quad (4)$$

To estimate the mass of a typical star cluster, we consider the sample of 9 starburst galaxies studied by Meurer et al. (1995) (see also Maoz et al. 2001). They found that the compact star clusters had minimum masses in the range $6 \times 10^3\text{--}2.4 \times 10^5 M_\odot$ assuming a

Salpeter IMF in the range $5\text{--}100 M_{\odot}$. By extending the lower mass limit to $0.1 M_{\odot}$, this range increases to $3.3 \times 10^4\text{--}1.3 \times 10^6 M_{\odot}$. We adopt $10^5 M_{\odot}$ as representative of the typical mass. For clusters of this mass the Lyc production rate per cluster at 1 Myr is $Q_{\text{Lyc}}/N_{\text{clus}} = 9 \times 10^{51} \text{ s}^{-1}$. For $Q_{\text{H}_2}/Q_{\text{Lyc}} = 0.5$, and n_e between 100 and 10^3 cm^{-3} the FUV flux ranges from 2×10^3 to 4×10^4 .

We note that the electron densities in ULIRGs reported by Veilleux et al. (1999) have a distribution which peaks at values around $100\text{--}200 \text{ cm}^{-3}$ with a long tail to higher values, and a few above 1000 cm^{-3} . However, it is not clear whether these densities, which are derived from the $[\text{SII}]\lambda 6716/\lambda 6731$ doublet measured in a $\sim 2 \times 4 \text{ kpc}$ aperture, do trace the density in the inner star forming regions or whether they are dominated by more extended emission. In the latter case, the emission could arise in diffuse gas at relatively large radii, e.g. in superwinds, and would thus provide only a lower limit on the central density. The density profiles for a number of galaxies with superwinds have been measured by Heckman et al. (1990). They find that at large radii, greater than a few kpc for the more luminous galaxies (which include several ULIRGs), the density is consistent with a r^{-2} profile and has a value of 100 cm^{-3} at some point typically within $r \sim 1\text{--}3 \text{ kpc}$. But n_e attains a more constant value in the range $500\text{--}1000 \text{ cm}^{-3}$ at smaller radii.

In summary we conclude that our $\text{Br}\gamma$ and H_2 line fluxes are consistent with nuclear star forming clusters containing massive stars, with ages $\sim 1 \text{ Myr}$ for instantaneous bursts, or more evolved $5\text{--}10 \text{ Myr}$ systems for continuous star formation. The H_2 line fluxes, and corresponding FUV-band photon production rates, are consistent with the intense FUV fluxes, $\chi = 10^3\text{--}10^5$ we adopted in our PDR models 2, 4, and 5. As we have seen, the H_2 line ratios imply that the PDRs are dense, with n_{H} between 10^4 and 10^6 cm^{-3} , and hot, with $T = 1000\text{--}1500 \text{ K}$ in the outer edges.

4.2. Comparison of PDRs to Other Star Forming Regions

How do the physical conditions for the PDRs – UV intensity, temperature, density – that we have derived in Section 4.1 compare to those in other star forming regions?

One of the best studied PDRs is that in Orion. Several authors (e.g. Luhman et al. 1998; Marconi et al. 1998; Usuda et al. 1996) have found that in some regions of Orion there is clear evidence for dense PDRs illuminated by intense UV radiation. The integrated 1-0 S(1) luminosity within a few arcmin of $\theta^1 \text{ Ori C}$, which includes all these dense PDRs as well as some outflows with shocked emission, is only $4.9 L_{\odot}$ (Usuda et al. 1996). However, large scale observations of the Orion cloud suggest that the total 1-0 S(1) luminosity is at

least $34 L_\odot$ and over the entire $\sim 3^\circ \times 10^\circ$ CO cloud may be as much as $63 L_\odot$ (Luhman et al. 1994). That is, the extended emission dominates the total emission by a factor of 7–13. Based on the surface brightness ($1.4 \times 10^{-9} \text{ W m}^{-2} \text{ sr}^{-1}$) and the strength of the 6-4 Q(1) line at $1.601 \mu\text{m}$ ($1\text{-}0 \text{ S}(1)/6\text{-}4 \text{ Q}(1) = 2.9$) in the extended emission, the authors concluded that the excitation mechanism is fluorescence by a weak UV field in low density PDRs, similar to our PDR model 1. Hence, although Orion does contain a number of dense intensely illuminated PDRs, on a global scale – i.e. if it were observed from far enough away to be spatially unresolved – its measured properties would be those of the extended emission. Hence, it does *not* appear to be similar to the PDRs in ULIRGs. By analogy, one would might speculate that in ULIRGs there are some PDRs which have much greater (or smaller) densities and incident UV fields than the global properties we have been able to measure, but that these account for only a small fraction of the total H_2 luminosity.

The extended emission in the inner 400 pc of the Galaxy is different to that in Orion. Pak et al. (1996) found that although there is very intense emission close to Sgr A, the emission extended on degree scales has a lower surface brightness of $\sim 3 \times 10^{-8} \text{ W m}^{-2} \text{ sr}^{-1}$ (corrected for foreground extinction of $A_K = 2.5$), although this is still an order of magnitude higher than that in Orion. Based on this and the uniformity of the emission, the authors concluded that it was excited in moderately dense PDRs with moderate UV field – similar to our PDR model 2, which has a similar density to but a lower UV intensity than we have observed in ULIRGs. Table 3 shows that the intrinsic surface brightness of 1-0 S(1) emission is similar in both cases.

The 400 pc scale over which these measurements were made is similar to that covered by our $0.75''$ aperture at the distance of the ULIRGs. The 1-0 S(1) line luminosities for the ULIRGs given in Table 2 has a mean of $2 \times 10^6 L_\odot$ without extinction or aperture corrections. Including this correction factor, we find that the line luminosity is 3–4 orders of magnitude greater than the $8000 L_\odot$ (already corrected for extinction) measured in the Galactic Center (Pak et al. 1996). Since we have shown that the surface brightness of the individual PDRs is similar both in the Galactic Center and in ULIRGs, the difference in total H_2 luminosity must be due to a vast increase in the filling factor of the PDRs.

We argue that this is due not only to an increase in the number of molecular clouds, but also an increase in the number of molecular clouds that have become PDRs. The gas mass in the inner 500–600 pc of the Galaxy has been determined by a variety of means including $^{12}\text{CO}(1\text{-}0)$ and $\text{C}^{18}\text{O}(1\text{-}0)$ radio measurements, thermal dust emission detected by IRAS and COBE, and 0.1–1.0 GeV γ -rays (see Dahmen et al. 1998, and references therein). These all yield similar values, for which the authors estimated the weighted mean to be $3 \times 10^7 M_\odot$. Typically, ULIRGs have a strong central concentration of molecular gas on the order of

$10^{9-10} M_{\odot}$, for example as deduced from observations of the CO(1-0) line by Evans et al. (2002) with a 2–4" beam and for a much larger sample, but also with a larger beam of 13–22", by Solomon et al. (1997). For the 3 ULIRGs in this paper for which the radio CO 1-0 luminosities have been measured, the derived gas masses are $1.5-2.0 \times 10^{10} M_{\odot}$ (Mirabel et al. 1990). These results indicate that the ratio $L_{1-0\text{S}(1)}/M_{\text{gas}}$ is 10–100 times greater in ULIRGs than in the Galactic Center, implying a much higher star formation efficiency for the ULIRGs (c.f. Sanders & Mirabel 1996, and references therein).

5. Spatial Variation of Line Flux

In Section 4 we have discussed only the line emission in the centre of the ULIRGs. Figure 5 shows that in many cases it is extended beyond this, and with a 1-0S(1)/Br γ ratio which varies considerably from that in the nucleus. In Figure 6 we show position-velocity diagrams for the objects, which show that (where it can be observed) the 1-0S(1) line has the same velocity characteristics as the Br γ line, suggesting that the two lines arise from similar regions. In contrast if, for example, the H₂ emission arose from material blown out or shocked in a superwind (e.g. as for NGC 253, Sugai et al. 2003) one might expect to see broader or double-peaked profiles similar to those observed in the H α lines by Heckman et al. (1990). However, since the line intensity is very low in the circumnuclear regions, we cannot rule out this possibility.

MCG –03–04–014 appears to be unique among these objects in having the brightest Br γ knots offset from the nucleus by 1–2" (0.7–1.4 kpc). This indicates that there is significant recent star formation in the circumnuclear region. At these locations the 1-0S(1)/Br γ ratio has decreased by a factor of 3 with respect to that in the nucleus, perhaps indicative of lower PDR gas densities.

In many of the other ULIRGs, particularly IRAS 01364–1042 and IRAS 14378–3651, there is evidence that the 1-0S(1)/Br γ ratio increases in the circumnuclear region, although the surface brightness diminishes rapidly. In IRAS 01364–1042 the ratio of 1-0S(1) to the continuum peaks at radii of 0.5–1.0" (0.5–1.0 kpc), while the Br γ distribution is very centralised. As in MCG –03–04–014, the reduction in 1-0S(1) surface brightness could be due to lower gas densities in the PDRs. IRAS 16164–0746 appears to have very broad extended line emission with little change in the 1-0S(1)/Br γ ratio over at least 2" (1.1 kpc). The continuum emission is also broad, with a spatial FWHM of 1.4" (0.8 kpc). The image in Fig. 1 shows that the slit was aligned close to the position angle of a prominent bar, and this may be influencing the observed size of the nucleus.

Since the slit position angles for all the objects were assigned rather arbitrarily (due to the quality of previously available images) and in most cases do not lie along either the major or the minor axis of the galaxy, it is difficult to draw strong conclusions about the extended emission. However, it is clear that the characteristics of the emission lines (strength and ratios) change in the circumnuclear region, and hence the excitation conditions must also change.

6. Conclusions

We have presented K-band spectra of 7 ULIRGs. Fitting stellar templates to line-free parts of the spectra has allowed us to fit and remove the absorption features in order to improve our detection limit for faint lines. We have measured line fluxes of $\text{Br}\gamma$ and H_2 lines from the $\nu = 1, 2$, and 3 levels, and conclude the following:

- (1) The nuclear H_2 line ratios show very little variation between the objects, suggesting that the excitation mechanism and conditions are similar in all cases, at least in the nuclei. However, the 1-0 S(1) and $\text{Br}\gamma$ line ratio and equivalent widths vary away from the nucleus, suggesting that in the circumnuclear region the excitation mechanisms may be different, perhaps as a result of a different evolutionary phase of the star formation.
- (2) We find that neither shocks nor models of low density PDRs can satisfactorily fit the nuclear H_2 line ratios; but FUV-pumped gas in high density PDRs can account for the observed ratios and fluxes. Parameter ranges that produce PDR models consistent with the observed H_2 line ratios are: gas densities $n_{\text{H}} = 10^{4-5} \text{ cm}^{-3}$, temperatures at the outer edge of the clouds $T \approx 1000 \text{ K}$, and illuminating FUV fields $\chi = 10^3-10^5$ times more intense than the local interstellar field.
- (3) We have constructed a simple model of star formation based on fluorescence of gas in PDRs at the edge of HII regions surrounding compact star clusters. This model can account for the ratios of the HeI, $\text{Br}\gamma$, and fluorescent H_2 line intensities, and implies young (1–5 Myr) clusters containing massive (120 M_\odot) stars. Our model implies that the nuclear K-band continuum is dominated by a separate older stellar population.
- (4) The PDRs in ULIRGs and those in the inner few hundred parsecs of the Galaxy have similar 1-0 S(1) surface brightnesses. Since the 1-0 S(1) emission in both cases is predominantly from PDRs, the quantity $L_{1-0 \text{ S}(1)}/M_{\text{gas}}$ traces the ratio of the number of PDRs to the number of molecular clouds – i.e. the star formation efficiency. This ratio is 10–100 times larger in ULIRGs than in the Galactic Center.

The authors are grateful to the staff at the Paranal Observatory for carrying out in service mode the observations presented in this paper. We thank the German-Israeli Foundation (grant I-0551-186.07/97) for support. We thank R. Genzel, D. Lutz, and the referee for comments and helpful suggestions.

REFERENCES

Black J., van Dishoeck E., 1987, *ApJ*, 322, 412

Bottorff M., Lamothe J., Momjian E., Verner E., Vinkovic D., Ferland G., 1998, *PASP*, 110, 1040

Burton M., Hollenbach D., Haas M., Erickson E., 1990a, *ApJ*, 355, 197

Burton M., Hollenbach D., Tielens A., 1990b *ApJ*, 365, 620

Chang C., Martin P., 1991, *AJ*, 378, 202

Coziol R., Doyon R., Demers S., 2001, *MNRAS*, 325, 1081

Dahmen G., Hüttenmeister S., Wilson T., Mauersberger R., 1998, *A&A*, 331, 959

Davies R., Sugai H., Ward M., 1998, *MNRAS*, 295, 43

Davies R., Ward M., Sugai H., 2000, *ApJ*, 535, 735

Doyon R., Wright G., Joseph R., 1994, *ApJ*, 421, 115

Draine B., 1978, *ApJS*, 36, 595

Draine B., 2003, *ARA&A*, in press

Draine B., Woods, D., 1990, *ApJ*, 363, 464

Draine B., Bertoldi F., 1996, *ApJ*, 468, 269

Evans A., Mazzarella J., Surace J., Sanders D., 2002, *ApJ*, 580, 749

Genzel R., Weitzel L., Tacconi-Garman L., Blietz M., Cameron M., Krabbe A., Lutz D., Sternberg A., 1995, *ApJ*, 498, 579

Genzel R., et al., 1998, *ApJ*, 498, 579

Gilbert A., et al., 2000, *ApJ*, 533, L57

Goldader J., Joseph R., Doyon R., Sanders D., 1995 *ApJ*, 444, 97

Goldader J., Joseph R., Doyon R., Sanders D., 1997, *ApJS*, 108, 449

Heckman T., Armus L., Miley G., 1990, *ApJS*, 74, 833

Howarth I., 1983, *MNRAS*, 203, 301

Koester D., Stoerzer H., Stutzki J., Sternberg A., 1994, *A&A*, 284, 545

Leitherer C., et al., 1999, *ApJS*, 123, 3

Lim A., Raga A., Rawlings J., Williams D., 2002, *MNRAS*, 335, 817

Luhman K., Engelbracht C., Luhman M., 1998 *ApJ*, 499, 799

Luhman M., Jaffe D., Keller L., Pak S., 1994, *ApJ*, 436, L185

Maoz D., Barth A., Ho L., Sternberg A., Filippenko A., 2001, *AJ*, 121, 3048

Marconi A., Testi L., Natta A., Walmsley C., 1998 *A&A*, 330, 696

Meurer G., Heckman T., Leitherer C., Kinney A., Robert C., Garnett D., 1995, *AJ*, 110, 2665

Mihos C., Hernquist L., 1996, *ApJ*, 464, 641

Mirabel I.F., Booth R., Garay G., Johansson L., Sanders D., 1990, *A&A*, 236, 327

Murphy T., Soifer B., Matthews K., Armus L., Kiger J., 2001, *AJ*, 121, 97

Osterbrock D., 1989, in *Astrophysics of Gaseous Nebulae and Active Galactic Nuclei*, University Science Books, Sausalito, USA

Pak S., Jaffe D., Keller L., 1996, *ApJ*, 457, L43

Puxley P., Hawarden T., Mountain M., 1988, *MNRAS*, 234, P29

Sanders D., Mirabel F., 1996, *ARA&A*, 34, 749

Shields J., 1993, *ApJ*, 419, 181

Smits, D., 1991, *MNRAS*, 248, 193

Solomon P., Downes D., Radford S., Barrett J., 1997, *ApJ*, 478, 144

Sternberg A., 1988, 332, 400

Sternberg A., Dalgarno A., 1989, *ApJ*, 338, 197

Sternberg A., Dalgarno A., 1995, *ApJS*, 99, 565

Sternberg A., 1998, *ApJ*, 506, 721

Sternberg A., Neufeld D., 1999, *ApJ*, 516, 371

Sternberg A., Hoffmann T., Pauldrach A., *ApJ*, submitted

Sugai H., Davies R., Ward M., 2003, *ApJ*, 584, L9

Sugai H., Malkan M., Ward M., Davies R., McLean I., 1997 *ApJ*, 481, 186

Tacconi-Garman L., Sternberg A., Eckart A., 1996, *AJ*, 112, 918

Tielens A., Hollenbach D., 1985, *ApJ*, 291, 722

Timmermann R., Bertoldi F., Wright C., Drapatz S., Draine B., Haser L., Sternberg A., 1996, *A&A*, 315, L281

Timmermann R., 1998, *ApJ*, 498, 246

Thornley M., Förster Schreiber N., Lutz D., Genzel R., Spoon H., Kunze D., Sternberg A., 2000 *ApJ*, 539, 641

Thronson H., Greenhouse M., 1988, *ApJ*, 327, 671

Tokunaga A., 2000, in *Allen's Astrophysical Quantities, Fourth Edition*, ed. Cox. A., Springer (New York)

Usuda T., Sugai H., Kawabata H., Inoue M., Kataza H., Tanaka M., 1996, *ApJ*, 464, 818

Veilleux S., Kim D.-C., Sanders D., 1999, *ApJ*, 522, 113

Voit G., 1992, *ApJ*, 399, 495

Wallace L., Hinkle K., 1997, *ApJS*, 111, 445

Wilgenbus D., Cabrit ., Pineau des Forêts G., Flower, D., 2000 *A&A*, 356, 1010

Wolniewicz L., Simbotin I., Dalgarno A., 1998, *ApJS*, 115, 293

Table 1. Basic Data for the Galaxies Observed

object	RA (J2000)	dec (J2000)	cz (km s ⁻¹)	S ₁₂ (Jy)	S ₂₅ (Jy)	S ₆₀ (Jy)	S ₁₀₀ (Jy)
MCG –03–04–014	01 10 08.9	–16 51 10	10040	0.301	0.846	6.48	10.44
IRAS 01364–1042	01 38 52.9	–10 27 12	14520	<0.077	0.396	6.16	6.70
MCG –03–12–002 ^a	04 21 20.0	–18 48 39	9652	0.185	0.430	5.75	8.20
IRAS 14378–3651	14 40 59.4	–37 04 33	20277	<0.116	0.525	6.19	6.34
IRAS 16164–0746	16 19 11.9	–07 54 03	8140	<0.350	0.562	10.20	13.72
IRAS 19458+0944	19 48 15.5	+09 52 02	29964	<0.250	<0.278	3.95	7.11
IRAS 20414–1651 ^b	20 44 17.4	–16 40 14	26107	<0.647	0.346	4.36	5.25

^aMCG –03–12–002 is a pair with a separation of 17''; we observed only the northern component, to which the IRAS data is closer.

^bIRAS 20414–1651 has two nuclei separated by 2.6'', of which only one is visible in the K-band.

Note. — IRAS data is from the Faint Source Catalogue and Point Source Catalogue

Table 2. Measured Data

object	Distance ^a (Mpc)	K-mag	$F_{S(1)}$ ^b $10^{-18} \text{ W m}^{-2}$	$\log \frac{L_{S(1)}}{L_\odot}$
MCG –03–04–014	145	13.4	2.85	6.27
IRAS 01364–1042	210	13.4	2.03	6.45
MCG –03–12–002	139	15.0	0.53	5.51
IRAS 14378–3651	294	14.7	0.93	6.40
IRAS 16164–0746	117	13.2	1.20	5.71
IRAS 19458+0944	438	14.4	1.90	7.06
IRAS 20414–1651	381	13.8	1.01	6.66

^aLuminosity distance calculated using $H_0 = 70 \text{ km s}^{-1} \text{ Mpc}^{-1}$ and $q_0 = 0.5$.

^b1-0 S(1) line flux extracted in a $0.75''$ length of a $1.00''$ slit; errors are given with the line ratios in Table 4.

Table 3. Parameters for the H_2 PDR Models

model	χ	n_{H} (cm^{-3})	T_{max} ^a (K)	$I_{1-0\text{S}(1)}$ ^b ($\text{W m}^{-2} \text{ sr}^{-1}$)	I_{H_2} ^c ($\text{W m}^{-2} \text{ sr}^{-1}$)
1	10^2	10^3	10^2	1.29×10^{-9}	7.06×10^{-8}
2	10^3	10^4	10^3	5.17×10^{-8}	2.88×10^{-6}
3	10^3	10^4	2×10^3	2.00×10^{-6}	3.22×10^{-5}
4	10^5	10^4	10^3	7.41×10^{-8}	4.04×10^{-6}
5	10^5	10^6	10^3	8.82×10^{-7}	1.80×10^{-5}

^aFor model 1 $T = 100 \text{ K}$ at all cloud depths. For the other models, the temperature varies as given in Eq. 1.

^bThe 1-0 S(1) intensity is that predicted by the model. Intensities for other lines can be found by using the model line ratios given in Table 4.

^cThe total H_2 intensity summed over all the H_2 lines is that predicted by the model.

Table 4. Relative Line Fluxes

object/model	1 σ ^a	line and wavelength (μm)									
		1-0S(2) 2.0338	He I 2.0587	3-2S(5) 2.0656	2-1S(3) 2.0735	1-0S(1) 2.1218	2-1S(2) 2.1542	Br γ 2.1661	3-2S(3) 2.2014	1-0S(0) 2.2233	2-1S(1) 2.2477
MCG –03–04–014	0.053	0.354	0.316	<0.160	0.128	1.000	<0.160	1.254	<0.160	0.298	0.194
IRAS 01364–1042	0.016	0.365	0.282	<0.048	0.139	1.000	0.066	0.600	0.062	0.262	0.140
MCG –03–12–002	0.042	0.335	0.221	<0.126	0.173	1.000	0.078	0.657	0.088	0.218	0.113
IRAS 14378–3651	0.034	0.325	0.459	<0.103	0.144	1.000	<0.103	1.153	<0.103	0.268	—
IRAS 16164–0746	0.022	—	0.665	<0.065	0.169	1.000	0.078	1.331	0.079	0.321	0.138
IRAS 19458+0944	0.052	0.317	0.386	<0.157	0.155	1.000	<0.157	1.038	—	—	—
IRAS 20414–1651	0.061	0.328	0.348	<0.183	0.113	1.000	<0.183	0.797	<0.183	0.258	0.123
mean H ₂ ratios	0.337		<0.120	0.146	1.000	0.074		0.076	0.271	0.142	
std. dev. of ratios	0.018			0.022		0.007		0.013	0.035	0.031	
thermal: 1000 K	0.27		0.00	0.00	1.00	0.00		0.00	0.27	0.01	
2000 K	0.37		0.00	0.08	1.00	0.03		0.01	0.21	0.08	
PDR ^b : model 1	0.49		0.02	0.22	1.00	0.25		0.10	0.54	0.53	
model 2	0.32		0.04	0.15	1.00	0.08		0.07	0.33	0.17	
model 3	0.35		0.00	0.05	1.00	0.02		0.00	0.22	0.05	
model 4	0.31		0.05	0.16	1.00	0.08		0.07	0.32	0.17	
model 5	0.29		0.02	0.10	1.00	0.04		0.04	0.33	0.11	

^aThe 1 σ error applies to all line fluxes given, including 1-0S(1). It is measured directly from the spectrum as the RMS of the residual after subtraction of both the stellar continuum and emission lines.

^bFor details of the PDR models, see Table 3.

Note. — Lines with no ratio given were not within the wavelength covered; 3 σ upper limits are given for lines within this range that were not detected.

Table 5. Derived Data

object	$\log \frac{L_{bol}}{L_\odot}$ ^a	$\log \frac{L_K}{L_\odot}$	$\log \frac{Q_{\text{Ly}\alpha}}{\text{ph s}^{-1}}$	$\frac{Q_{\text{H}_2}}{Q_{\text{Ly}\alpha}}$ ^b	$100 \times \frac{Q_{\text{He}}^{\text{min}}}{Q_{\text{Ly}\alpha}}$ ^b
MCG –03–04–014	11.62	8.83	53.82	0.33 ± 0.06	1.92 ± 0.06
IRAS 01364–1042	11.79	9.15	53.68	0.75 ± 0.01	3.58 ± 0.01
MCG –03–12–002	11.48	8.15	52.78	0.86 ± 0.05	2.56 ± 0.10
IRAS 14378–3651	12.09	8.93	53.91	0.41 ± 0.02	3.03 ± 0.02
IRAS 16164–0746	11.52	8.72	53.29	0.41 ± 0.01	3.80 ± 0.01
IRAS 19458+0944	12.27	9.39	54.53	0.48 ± 0.06	2.83 ± 0.06
IRAS 20414–1651	12.18	9.51	54.02	0.46 ± 0.14	3.33 ± 0.12

^a L_{bol} is calculated from the IRAS fluxes for the range 8–1000 μm , using the formula given in Tokunaga (2000).

^b Q_{H_2} is calculated from a fluorescently excited H₂ line for PDR model 2. Quoted errors include uncertainties in both rates.

Table 6. Star Formation Models

age (Myr)	$\log \frac{L_K}{L_\odot}$	$\log \frac{Q_{\text{Lyc}}}{\text{ph s}^{-1}}$	$\frac{Q_{\text{H}_2}}{Q_{\text{Lyc}}}$	$100 \times \frac{Q_{\text{He}}}{Q_{\text{Lyc}}}$	$\log \frac{L_{\text{bol}}}{L_\odot}$
Instantaneous, cluster mass $10^5 M_\odot$, Salpeter IMF, $M_{\text{upper}} = 120 M_\odot$					
1	5.48	51.95	0.63	19.02	8.27
5	5.06	50.78	5.12	1.51	7.89
10	5.70	49.24	61.85	0.28	7.48
Instantaneous, cluster mass $10^5 M_\odot$, Salpeter IMF, $M_{\text{upper}} = 30 M_\odot$					
1	4.66	50.91	2.25	9.41	7.67
5	4.63	50.80	5.57	1.05	7.80
10	5.76	49.31	61.88	0.28	7.55
Continuous, $SFR = 1 M_\odot \text{ yr}^{-1}$, Salpeter IMF, $M_{\text{upper}} = 120 M_\odot$					
1	6.48	52.95	0.61	20.54	9.25
3	6.89	53.37	0.80	16.36	9.76
5	7.03	53.42	1.21	15.10	9.90
10	7.55	53.43	1.34	14.80	10.03
100	8.06	53.43	2.02	14.81	10.20
Continuous, $SFR = 1 M_\odot \text{ yr}^{-1}$, Salpeter IMF, $M_{\text{upper}} = 30 M_\odot$					
1	5.66	51.91	2.28	9.42	8.66
3	6.15	52.40	2.89	8.50	9.18
5	6.37	52.60	3.81	6.00	9.44
10	7.48	52.66	5.36	5.36	9.74
100	8.09	52.67	8.66	5.22	10.07

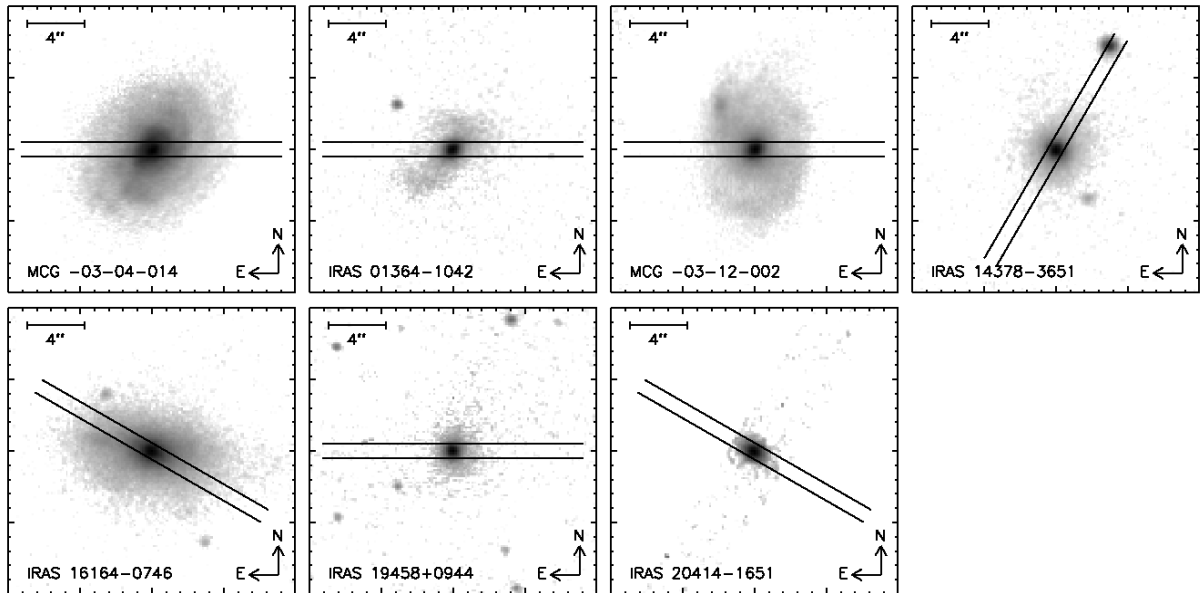


Fig. 1.— Acquisition images of the targets taken through a K_s filter (with the exception of IRAS 01364–1042 and IRAS 20414–1651, which were taken through a narrow-band $2.19\mu\text{m}$ filter due to the presence of a bright star in the ISAAC field of view). Each field is $20''\times20''$, and is drawn with logarithmic scaling. The parallel lines indicate the position angle and width of the slit. Due to cosmetic effects, only a narrow strip of the image for IRAS 20414–1651 is shown.

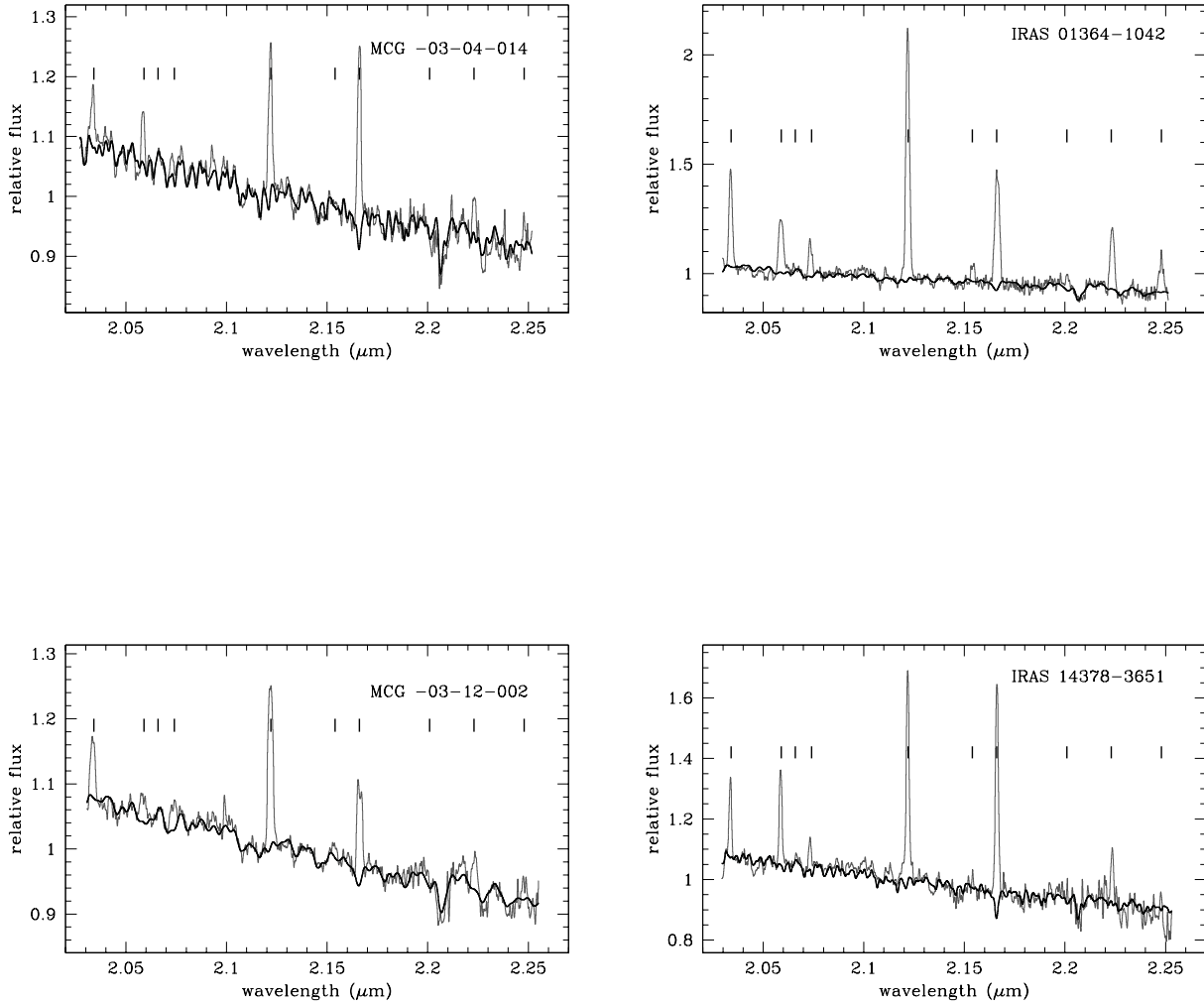
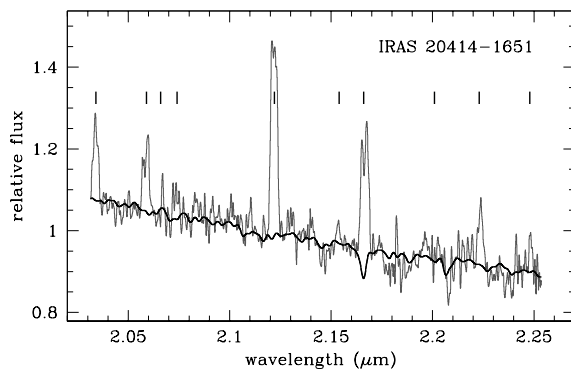
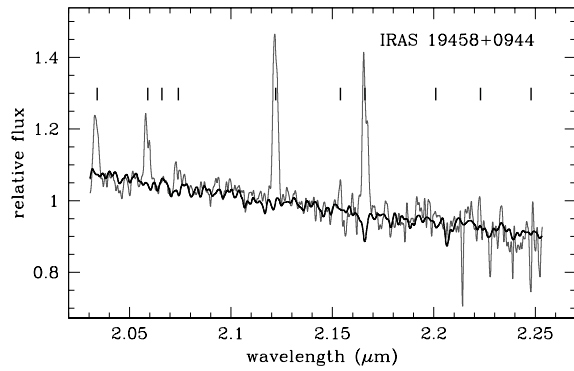
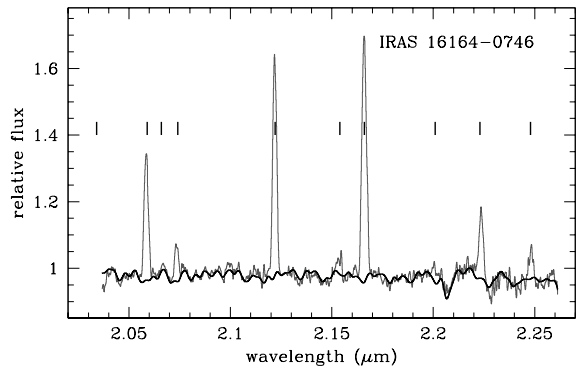


Fig. 2.— Spectra of each object, plotted at rest wavelength and normalised to their mean values. The thick overlaid line is the best fitting continuum constructed from stellar templates (see text for details). The vertical marks indicate the positions of the emission lines recorded in Table 4. Subtraction of the continuum is necessary in order to detect the faint lines such as 3-2S(3) at $2.2014\mu\text{m}$, which can be seen clearly in IRAS 01364–1042.



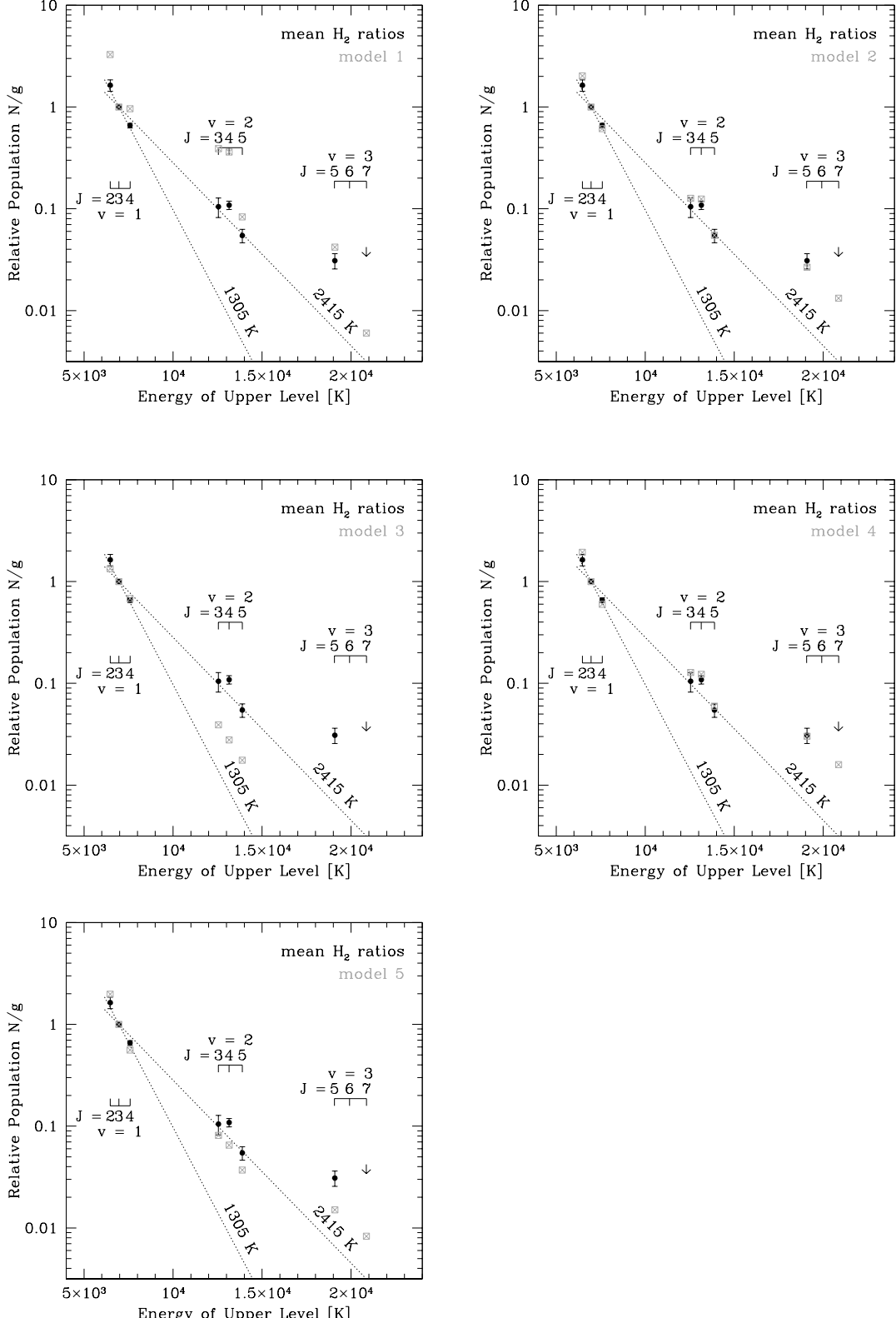


Fig. 3.— Excitation diagrams for the mean line ratios, and the 5 PDR models discussed in the text. Errors denote the standard deviation in the values used to calculate the mean; arrows denote mean of the 3σ upper limits. The two dotted lines indicate where the points for the best fitting purely thermal single temperature models would lie: the fits are to all the

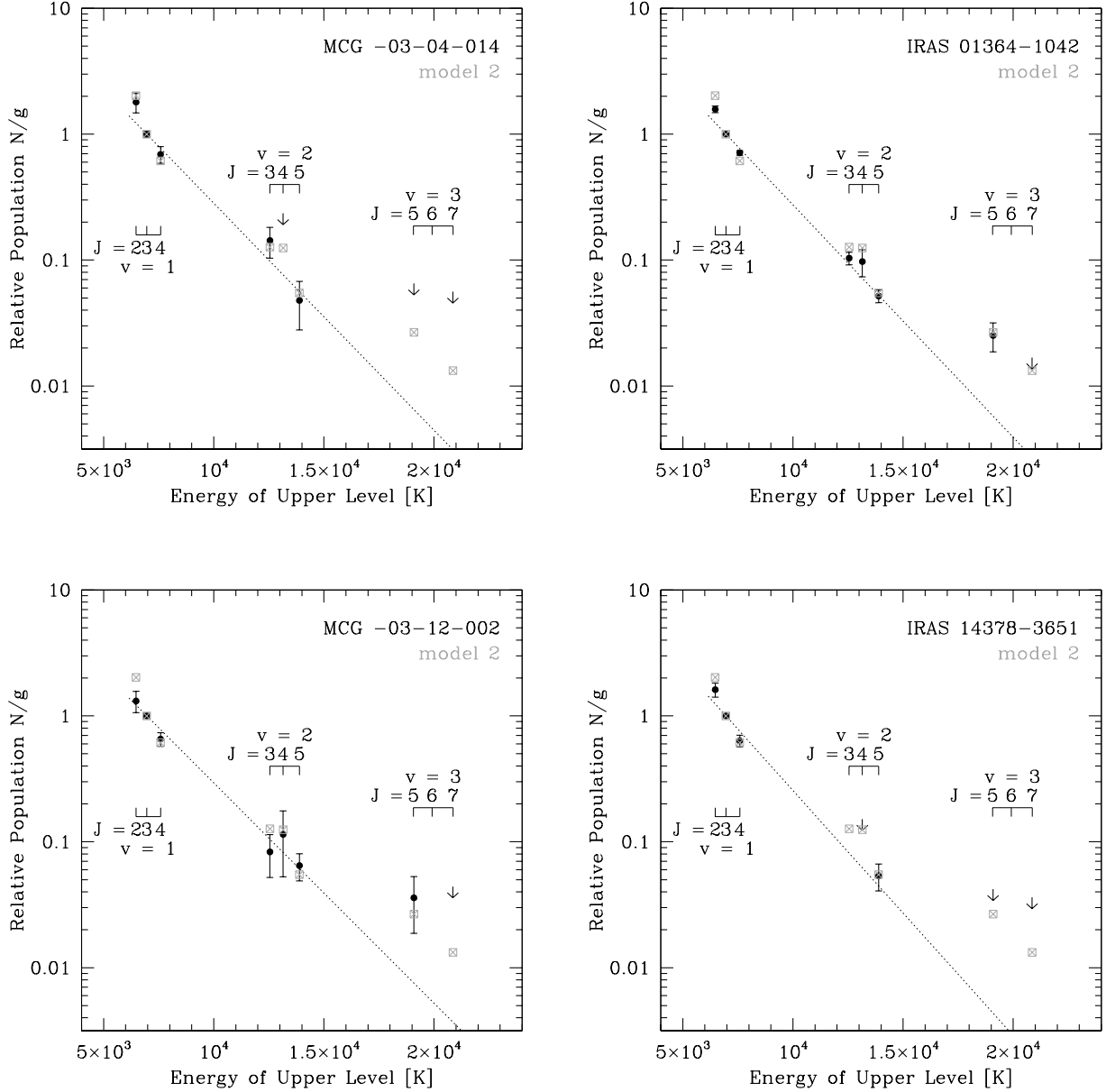
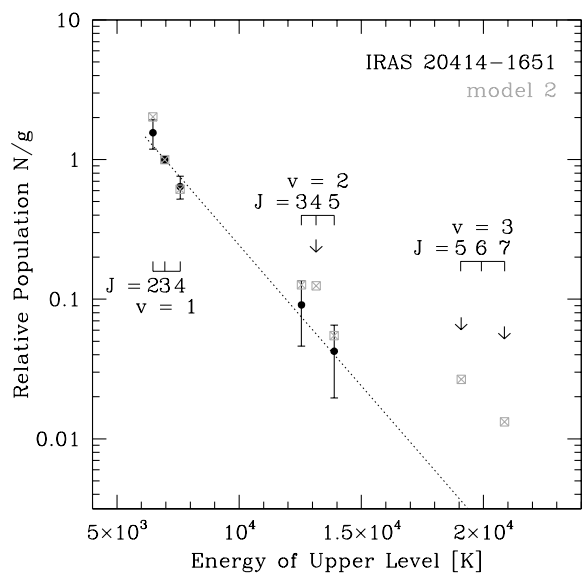
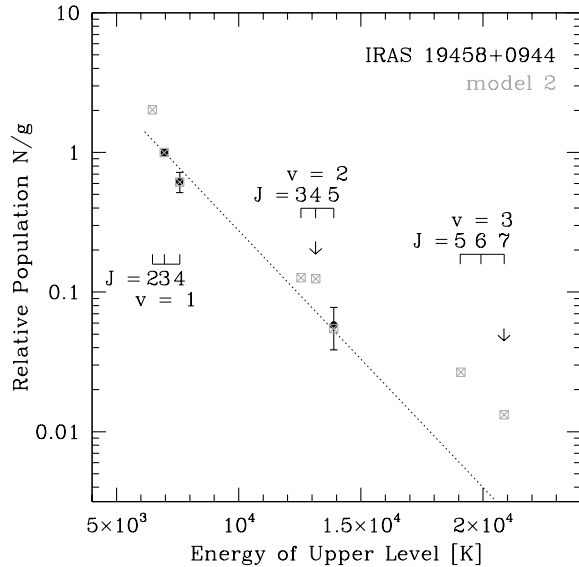
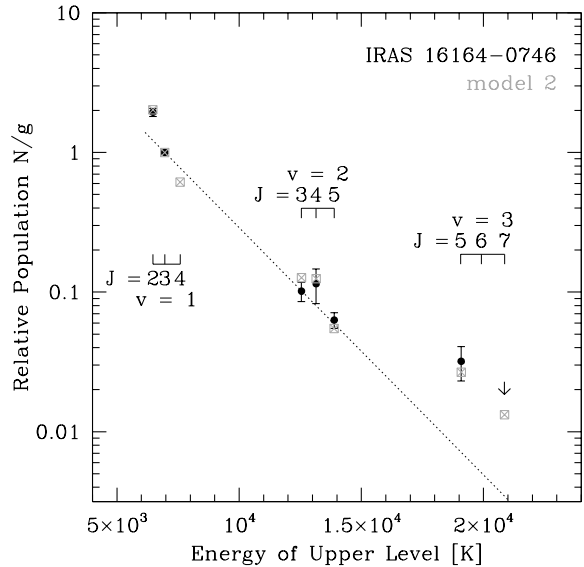


Fig. 4.— Excitation diagrams for the hot hydrogen molecules in each object. Arrows denote 3σ upper limits, derived from the residual spectrum after subtraction of the stellar continuum and line emission. The dotted lines indicate where the points for the best fitting purely thermal single temperature model would lie. The overlaid grey points show the populations for our PDR model 2.



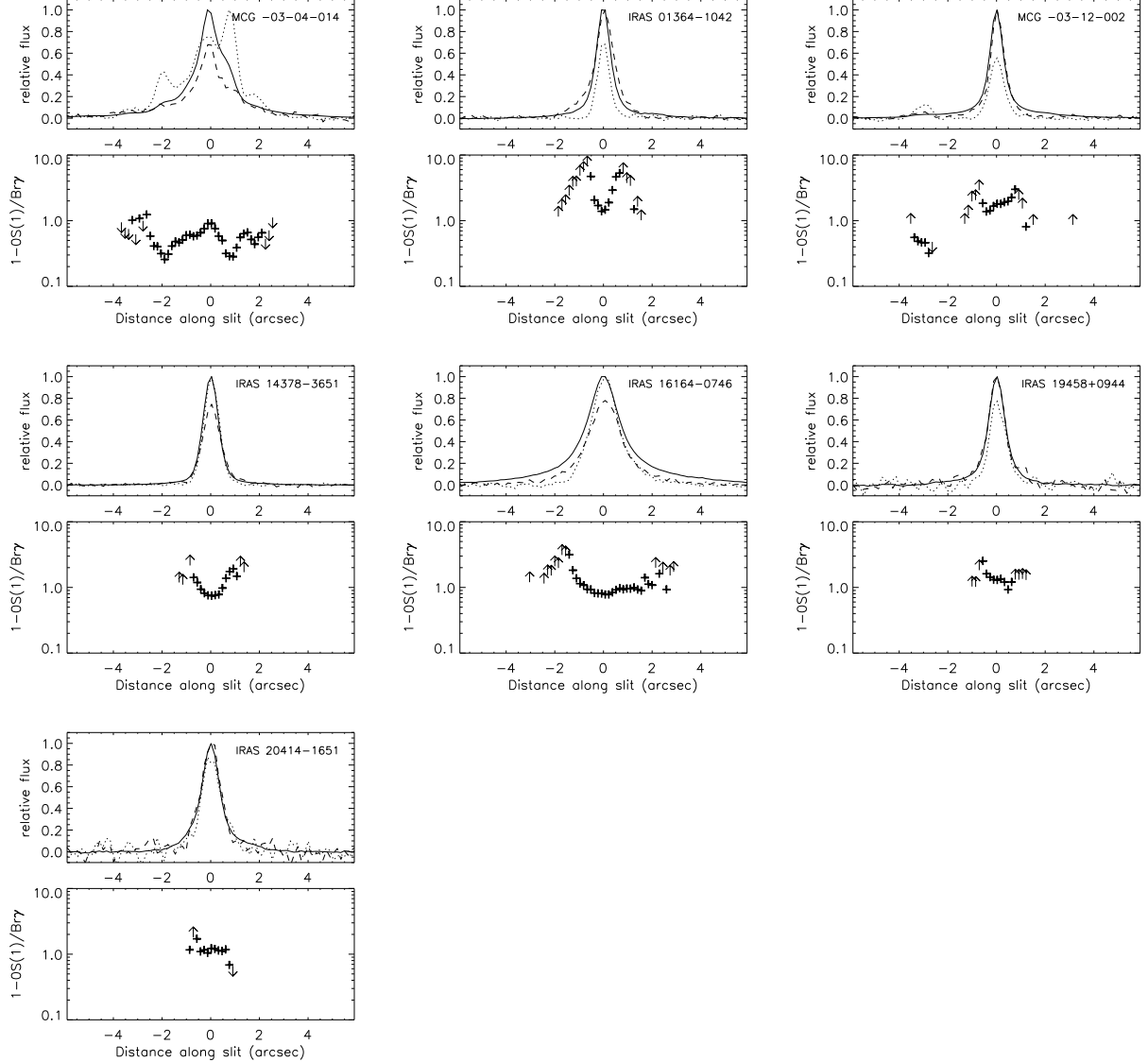


Fig. 5.— Upper: Normalised spatial distributions of the continuum flux density (solid line), the $\text{Br}\gamma$ flux (dotted line), and the 1-0S(1) flux (dashed line). A single normalisation was applied to the $\text{Br}\gamma$ and 1-0S(1) fluxes. Lower: 1-0S(1)/ $\text{Br}\gamma$ ratio (arrows denote 3σ limits).

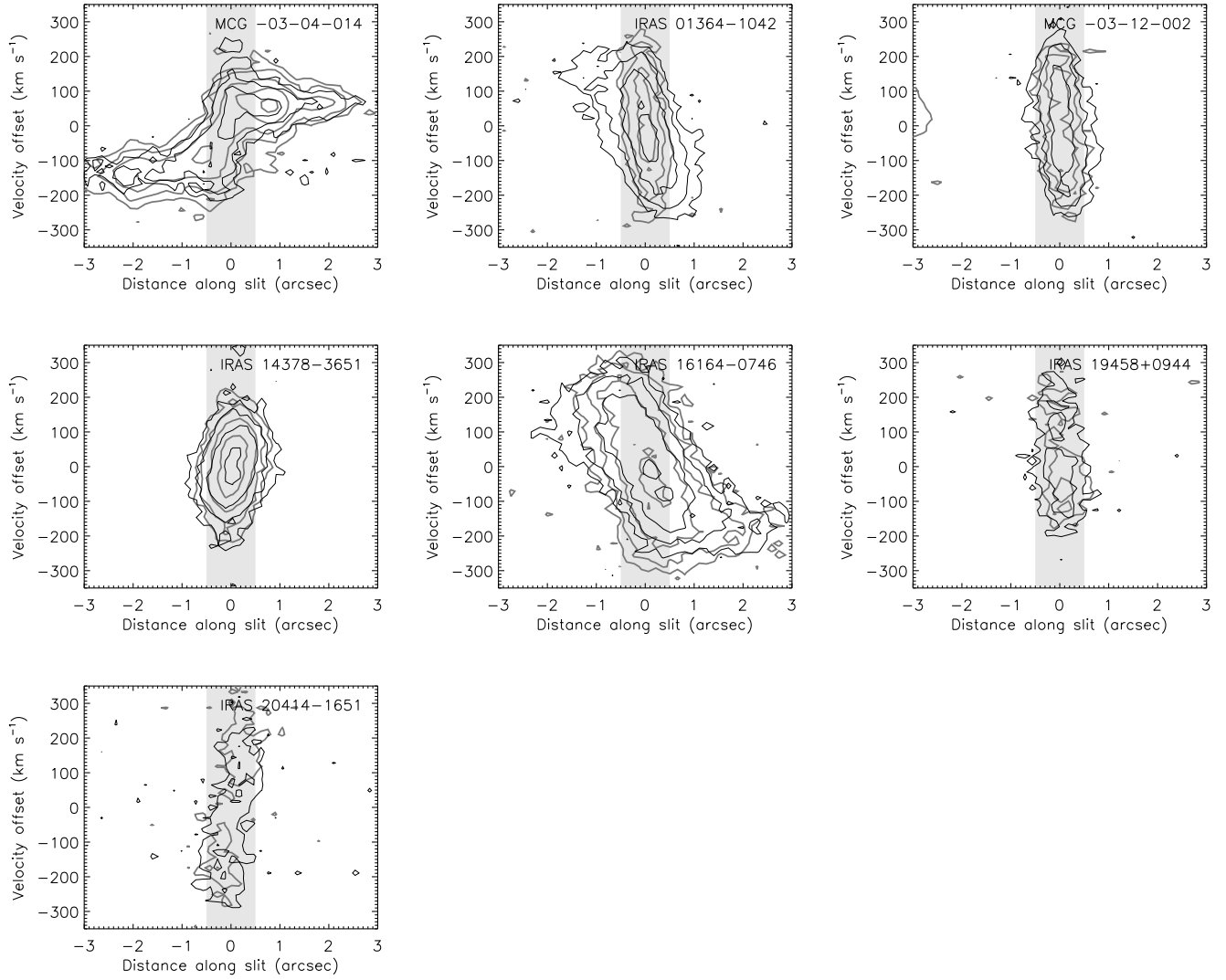


Fig. 6.— Position-velocity diagrams. The thick grey line is the Br γ , while the thin black line is for 1-0 S(1). The pale vertical stripe shows the region over which the spectra were extracted.